

A highly magnified candidate for a young galaxy seen when the Universe was 500 Myrs old

Wei Zheng¹, Marc Postman², Adi Zitrin³, John Moustakas⁴, Xinwen Shu⁵, Stephanie Jouvel^{6,7}, Ole Host⁶, Alberto Molino⁸, Larry Bradley², Dan Coe², Leonidas A. Moustakas⁹, Mauricio Carrasco¹⁰, Holland Ford¹, Narciso Benítez⁸, Tod R. Lauer¹¹, Stella Seitz¹², Rychard Bouwens¹³, Anton Koekemoer², Elinor Medezinski¹, Matthias Bartelmann³, Tom Broadhurst¹⁴, Megan Donahue¹⁵, Claudio Grillo¹⁶, Leopoldo Infante¹⁰, Saurabh Jha¹⁷, Daniel D. Kelson¹⁸, Ofer Lahav⁶, Doron Lemze¹, Peter Melchior¹⁹, Massimo Meneghetti²⁰, Julian Merten³, Mario Nonino²¹, Sara Ogaz², Piero Rosati²², Keiichi Umetsu²³, Arjen van der Wel²⁴

¹*Johns Hopkins University, 3701 San Martin Drive, Baltimore, MD 21218, U.S.A.*

²*Space Telescope Science Institute*

³*Universität Heidelberg*

⁴*University of California, San Diego*

⁵*University of Science and Technology of China*

⁶*University College London*

⁷*Institute de Ciencies de l'Espai*

⁸*Instituto de Astrofísica de Andalucía*

⁹*Jet Propulsion Laboratory, California Institute of Technology*

¹⁰*Pontificia Universidad Católica de Chile*

¹¹*National Optical Astronomical Observatory*

¹²*Universitas Sternwarte, München*

¹³*Leiden Observatory*

¹⁴*University of Basque Country*

¹⁵*Michigan State University*

¹⁶*Niels Bohr Institute, University of Copenhagen*

¹⁷*Rutgers University*

¹⁸*The Observatories of the Carnegie Institution for Science*

¹⁹*The Ohio State University*

²⁰*INAF-Osservatorio Astronomico di Bologna*

²¹*INAF-Osservatorio Astronomico di Trieste*

²²*European Southern Observatory*

²³*Academia Sinica, Institute of Astronomy & Astrophysics*

²⁴*Max-Planck Institut für Astronomie*

The early Universe at redshift $z \sim 6-11$ marks the reionization of the intergalactic medium, following the formation of the first generation of stars. However, those young galaxies at a cosmic age of $\lesssim 500$ million years (Myr, at $z \gtrsim 10$) remain largely unexplored as they are at or beyond the sensitivity limits of current large telescopes. Gravitational lensing by galaxy clusters enables the detection of high-redshift galaxies that are fainter than what otherwise could be found in the deepest images of the sky. We report the discovery of an object found in the multi-band observations of the cluster MACS1149+22 that has a high probability of being a gravitationally magnified object from the early universe. The object is firmly detected (12σ) in the two reddest bands of *HST*/WFC3, and not detected below $1.2 \mu\text{m}$, matching the characteristics of $z \sim 9$ objects. We derive a robust photometric redshift of $z = 9.6 \pm 0.2$, corresponding to a cosmic age of 490 ± 15 Myr (*i.e.*, 3.6% of the age of the Universe). The large number of bands used to derive the redshift estimate make it one of the most accurate estimates ever obtained for such a distant object. The significant magnification by cluster lensing (a factor of ~ 15) allows us to analyze the object's ultra-violet and optical luminosity in its rest-

frame, thus enabling us to constrain on its stellar mass, star-formation rate and age. If the galaxy is indeed at such a large redshift, then its age is less than 200 Myr (at the 95% confidence level), implying a formation redshift of $z_f \lesssim 14$. The object is the first $z > 9$ candidate that is bright enough for detailed spectroscopic studies with *JWST*, demonstrating the unique potential of galaxy cluster fields for finding highly magnified, intrinsically faint galaxies at the highest redshifts.

Observational cosmology has established that the age of the Universe is 13.7 billion years, and the reionization of the vast intergalactic medium (IGM) started around redshift $z \sim 11$,¹ as the result of radiation from the first generation of stars. The task of probing the most distant Universe is progressively challenging: While more than 10^5 quasars have been found, only one is at $z > 7$;² while thousands of gamma-ray burst events have been recorded, only one³ is confirmed at $z=8.3$; and while thousands of galaxy candidates have been found at $z \sim 6$, only one has been reported at $z \sim 10$,⁴ which is based on a single-band detection. Galaxies at $z \sim 10$ are expected to be at a magnitude of ~ 29 (in the AB system, used hereafter)^{4,5}, near the detection limits of the deepest fields observed by *Hubble Space Telescope* (*HST*), and beyond the spectroscopic capability of even the next generation of large telescopes.

In this *Letter* we report the discovery of a gravitationally lensed source whose most likely redshift is $z \sim 9.6$. The source, hereafter called MACS1149-JD1, is selected from a near-infrared detection image at significance of 22σ . MACS1149-JD1 has a unique flux distribution characterized by a) no detection at wavelengths shorter than $1.2 \mu\text{m}$, b) firm detections in the two reddest *HST* bands and c) weak detections in two other *HST*/WFC3/IR (Wide-Field Camera 3/Infrared Channel) bands and in one *Spitzer*/IRAC (Infrared Array Camera) channel. The object’s coordinates (J2000) are: RA= $11^{\text{h}}49^{\text{m}}33^{\text{s}}.584$ Dec= $+22^{\circ}24'45''.78$.

Galaxy clusters are the largest reservoirs of gravitationally bound dark matter (DM), whose huge mass bends light and forms “cosmic lenses.” They can significantly magnify the brightness and sizes of galaxies

far behind them, thereby revealing morphological details that are otherwise impossible to detect^{6–11} and enabling spectroscopy to study the physical conditions in these intrinsically faint galaxies. This is particularly important for the *Spitzer Space Telescope* infrared data where the telescope’s low spatial resolution blends faint sources. At $z > 7$, the $\text{Ly}\alpha$ break, at $\sim 0.12(1+z) \mu\text{m}$, is redshifted out off the optical bands, and the Balmer break, at $\sim 0.38(1+z) \mu\text{m}$, is redshifted into the *Spitzer*/IRAC range. By combining the *HST* and *Spitzer* data we are able to estimate the age of such distant objects based on the ratio of their rest-frame ultra-violet to optical fluxes. MACS1149-JD1 is approximately $15\times$ brighter than it would be in an unlensed field.

The Cluster Lensing And Supernova survey with Hubble (CLASH)¹² is a *HST* Multi-Cycle Treasury program that acquires images in 16 broad bands between $0.2–1.7 \mu\text{m}$ for 25 clusters. MACS J1149.6+2223 is a massive cluster at redshift $z = 0.544$, selected from a group of X-ray luminous clusters. The mass models for this cluster^{13,14} suggest a relatively flat mass distribution profile and a large area of high magnification, making it one of the most powerful cosmic lenses known.

The spectral-energy distribution (SED) features of galaxies, most notably the Lyman break and the Balmer break, generate distinct colors between broad bands and enable us to derive their redshifts with reasonable accuracy. Our photometric redshift estimates are made with two different techniques: Le Phare (LPZ)¹⁵ and Bayesian Photometric Redshifts (BPZ)¹⁶. LPZ photometric redshifts are based on a template fitting procedure with a maximum likelihood (χ^2) estimate. We use the template library of the COSMOS survey¹⁷, including galaxy templates of three ellipticals, seven spirals¹⁸ and 12 common templates¹⁹, with starburst ages ranging from 30 Myr to 3 Gyr (billion year) to better reproduce the bluest galaxies. The LPZ solution from the marginalized posterior is $z = 9.60^{+0.20}_{-0.28}$ (at 68% confidence level), and the best-fit model is a starburst galaxy.

BPZ multiplies the likelihood by the prior probability of a galaxy with an apparent magnitude m_0 of having a redshift z and spectral type T . We run BPZ using a new library composed of 11 SED templates originally drawn from PEGASE²⁰ but recalibrated using the FIREWORKS photometry and spectroscopic redshifts²¹ to optimize its performance. This galaxy library includes five templates for ellipticals, two for spirals, and four for starbursts. The most likely BPZ solution is a starburst galaxy at $z = 9.61^{+0.14}_{-0.13}$ (1σ).

Even though the CLASH data have more bands than other *HST* projects, MACS1149-JD1 is detected only in the four reddest *HST* bands. The high confidence of our high-redshift solution is enabled by the IRAC photometry at $3.6\mu\text{m}$ and $4.5\mu\text{m}$. With *HST* data alone (excluding *Spitzer* data) solutions with intermediate redshifts ($2 \lesssim z \lesssim 6$) can be found but they have low probability (Fig. 3). When *Spitzer* data are included, no viable solutions other than those at $z \sim 9.6$ are found, and the possibility for photometric redshifts $z < 8.5$ is rejected at 4σ confidence level ($< 3 \times 10^{-5}$).

Using confirmed multiply-lensed images, strong-lensing (SL) models^{13,22} allow us to derive the mass distribution of DM in the cluster, which leads to an amplification map for background sources. With 23 multiply-lensed images of seven sources, we derive the best-fit model in which the critical curve (of high magnification) of $z \sim 10$ extends to the vicinity of MACS1149-JD1, resulting in a magnification factor of $\mu = 14.5^{+4.2}_{-1.0}$. The results are in rough agreement with a second, independent model²³, which yields a best-fit magnification with large error bars, $26.6^{+20.8}_{-7.7}$.

Because our data cover a broad range in the object’s rest-frame, we are able to estimate some key properties for the source using the Bayesian SED-fitting code `iSEDfit`²⁴ coupled to state-of-the-art population synthesis models²⁵ and based on the Chabrier²⁶ initial mass function from $0.1 - 100 M_{\odot}$ (solar mass). We consider a wide range of parameterized star formation histories and stellar metallicities and assume no dust attenuation, as previous studies^{27,28} found no evidence for dust in galaxies at the highest redshifts.

Fig. 4 presents the results of our population synthesis modeling adopting $z = 9.6$ as the source redshift. Based on the median of the posterior probability distributions, our analysis suggests a stellar mass of $\sim 1.5 \times 10^8 (\mu/15)^{-1} M_\odot$ and a star-formation rate (SFR) of $\sim 1.2 (\mu/15)^{-1} M_\odot \text{ yr}^{-1}$. Given the uncertainties in the IRAC photometry, we are unable to measure the age of the galaxy precisely; however, we can constrain its SFR-weighted age, or the age at which most of the stars formed, to $\langle t \rangle_{\text{SFR}} < 200 \text{ Myr}$ (95% confidence level), suggesting a likely formation redshift $z_f < 14.2$. Given that the source is brighter at $4.5\mu\text{m}$ than at $3.6\mu\text{m}$, the presence of a Balmer break is likely, suggesting that MACS1149-JD1 may not be too young. This age implies a formation redshift of no earlier than $z_f \approx 11.3$, and is generally consistent with the estimated ages ($\gtrsim 100 \text{ Myr}$) of galaxies at slightly lower redshifts, $z \sim 7 - 8$.²⁹

MACS1149-JD1 is compact, but spatially resolved. We can get a clearer view of the source by removing the effects of *HST*'s point spread function (PSF) using Lucy-Richardson deconvolution^{37,38}. After deconvolution with the WFC3/IR PSF, the observed (*i.e.*, de-magnified) half-light radius of the core is $r < 0''.13$. The expected intrinsic size, based on extrapolations from measured galaxy sizes³⁰ from $z \sim 7$ to 10 in unlensed fields, is $r = 0''.07$. Assuming symmetrical amplification, MACS1149-JD1's magnified size would be $\sim 0''.25$ before convolution with the WFC3/IR PSF. This implies that the source is approximately half the size as expected. For comparison, if MACS1149-JD1 is at $z \sim 3$, its expected intrinsic size would be $0''.17$, and the expected observed size would be $0''.41$. The larger difference between the intermediate-redshift expectation and what we observe supports the high-redshift solution.

Methods summary

The presence of a prominent $\text{Ly}\alpha$ break caused by IGM absorption is used to identify high-redshift galaxy candidates. We select $z \sim 10$ candidates with the following criteria: (1) The difference in magnitude $\text{F110W} - \text{F140W} > 1.3$; (2) $\text{F140W} - \text{F160W} < 0.5$; and (3) No detection in the F105W band ($< 2\sigma$) and no

detection in the optical detection image ($< 1\sigma$). MACS1149-JD1 is the only object in our current database of 12 CLASH clusters observed to date that meets these criteria. We measure the photometry with a circular aperture of diameter 10 pixels ($0''.65$), and apply an aperture correction of -0.3 magnitude to infer the total galaxy magnitude measured with an aperture of 20 pixels.

We verify that MACS1149-JD1 is not a solar system object by placing an upper limit on its proper motion over the course of 80 days. The object is also inconsistent with being a late-type Galactic star – there are no L,M,T, or Y dwarfs whose total flux difference is within 6.8σ of the observed colors of MACS1149-JD1. The likelihood that the source is at an intermediate redshift is extremely low given the *Spitzer*/IRAC photometric constraints. We also study several pairs of flux ratios in different bands for all the objects in our CLASH database with similar magnitudes. The hypothesis that the source’s extremely red color is just due to photometric scatter of the general faint extragalactic population is excluded at 99.985% confidence level. More details are presented in the *Supplementary Information* section.

1. Komatsu, E., et al. Seven-year Wilkinson microwave anisotropy probe (WMAP) observations: cosmological interpretation, *Astrophys. J. Suppl.*, **192**, 18 (2011)
2. Mortlock, D. J., et al. A luminous quasar at a redshift of $z = 7.085$, *Nature*, **474**, 616-619 (2011)
3. Tanvir, N. R., et al. A γ -ray burst at redshift of $z \sim 8.2$, *Nature*, **461**, 1254-1257 (2009)
4. Bouwens, R. J., et al. A candidate redshift $z \approx 10$ galaxy and rapid changes in that population at an age of 500 Myr, *Nature*, **469**, 504-507 (2011)
5. Oesch, P. A., et al. Expanded search for $z \sim 10$ galaxies from HUDF09, ERS, and CANDELS data: evidence for accelerated evolution at $z > 8$? *Astrophys. J.*, **745**, 110 (2012)

6. Kneib, J.-P., Ellis, R. S., Santos, M. R. & Richard, J., A probable $z \sim 7$ galaxy strongly lensed by the rich cluster A2218: exploring the dark ages, *Astrophys. J.*, **607**, 697-703 (2004)
7. Bradley, L. D., et al. Discovery of a very bright strongly lensed galaxy candidate at $z \sim 7.6$, *Astrophys. J.*, **678**, 647-654 (2008)
8. Zheng, W., et al. Bright strongly lensed galaxies at redshift $z \sim 6 - 7$ behind the clusters Abell 1703 and CL0024+16, *Astrophys. J.*, **697**, 1907-1917 (2009)
9. Richard, J., et al. Discovery of a possibly old galaxy at $z = 6.027$, multiply imaged by the massive cluster Abell 383, *Mon. Not. R. Astron. Soc.*, **414**, L31-35 (2011)
10. Bradley, L. D., et al. Through the looking glass: bright, highly magnified galaxy candidates at $z \sim 7$ behind A1703, *Astrophys. J.*, **747**, 3 (2012)
11. Zitrin, A., et al. CLASH: Discovery of a bright $z \simeq 6.2$ dwarf galaxy quadruply lensed by MACS J0329.6-0211, *Astrophys. J.*, **747**, L9 (2012)
12. Postman, M., et al. Cluster lensing and supernova survey with Hubble (CLASH): an overview, *Astrophys. J. Suppl.*, **199**, 25 (2012)
13. Zitrin, A., & Broadhurst, T. Discovery of the largest known lensed images formed by a critically convergent lensing cluster, *Astrophys. J.*, **703**, L132-136 (2009)
14. Smith, G. P., et al. Hubble space telescope observations of a spectacular new strong-lensing galaxy cluster: MACS J1149.5+2223 at $z = 0.544$, *Astrophys. J.*, **707**, L163-168 (2009)
15. Ilbert, O., et al. Accurate photometric redshifts for the CFHT legacy survey calibrated using the VIMOS VLT deep survey, *A&Ap*, **457**, 841-856 (2006)
16. Benítez, N. Bayesian photometric redshift estimation, *Astrophys. J.*, **536**, 571-583 (2000)

17. Koekemoer, A. M., et al. The COSMOS survey: Hubble space telescope advanced camera for surveys observations and data processing, *Astrophys. J. Suppl.*, **172**, 196-202 (2007)
18. Polletta, M. Spectral energy distributions of hard X-Ray selected active galactic nuclei in the XMM-Newton medium deep survey, *Astrophys. J.*, **663**, 81-102 (2007)
19. Bruzual, G., & Charlot, S. Stellar population synthesis at the resolution of 2003, *Mon. Not. R. Astron. Soc.*, **344**, 1000-1028 (2003)
20. Fioc, M., & Rocca-Volmerange, B. PEGASE: a UV to NIR spectral evolution model of galaxies. application to the calibration of bright galaxy counts, *A&Ap*, **326**, 950-962 (1997)
21. Wuyts, S., et al., FIREWORKS U_{38} -to- $25\mu\text{m}$ photometry of the GOODS Chandra deep field-south: multiwavelength catalog and total infrared properties of distant K_s -selected Galaxies, *Astrophys. J. Suppl.*, **682**, 985-1003 (2008) dust-obscured galaxies of high- z dropout searches, *A&Ap*, **534**, 124 (2011)
22. Zitrin, A., Broadhurst, T., Barkana, R., Rephaeli, Y., & Benítez, N. Strong-lensing analysis of a complete sample of 12 MACS clusters at $z > 0.5$: mass models and Einstein radii, *Mon. Not. R. Astron. Soc.*, **410**, 1939-1956 (2011)
23. Jullo, E., et al. A Bayesian approach to strong lensing modelling of galaxy clusters, *New J. Phys.*, **9**, 447 (2007)
24. Moustakas, J., et al. Evolution of the stellar mass-metallicity relation since $z = 0.75$, *Astrophys. J.*, submitted (arXiv 1112.3300, 2011)
25. Conroy, C. & Gunn, J. E. The propagation of uncertainties in stellar population synthesis modeling. III. model calibration, comparison, and evaluation, *Astrophys. J.*, **712**, 833-857 (2010)

26. Chabrier, G. Galactic stellar and substellar initial mass function, *Pub. Astr. Soc. Pac.*, **115**, 763-795 (2003)
27. Labbé, I., et al. Ultradeep infrared array camera observations of sub- L^* $z \sim 7$ and $z \sim 8$ galaxies in the Hubble ultra deep field: the contribution of low-luminosity galaxies to the stellar mass density and reionization, *Astrophys. J.*, **708**, L26-31 (2010)
28. Bouwens, R. J., et al. Very blue UV-continuum slope β of low luminosity $z \sim 7$ galaxies from WFC3/IR: evidence for extremely low metallicities? *Astrophys. J.*, 708, L69-73 (2010)
29. Labbé, I., et al. Star formation rates and stellar masses of $z = 7 - 8$ galaxies from IRAC observations of the WFC3/IR early release science and the HUDF fields, *Astrophys. J.*, **716**, L103-108 (2010)
30. Oesch, P. A., et al. Structure and morphologies of $z \sim 7-8$ galaxies from ultra-deep WFC3/IR imaging of the Hubble ultra-deep field, *Astrophys. J.*, **709**, L21-25 (2010)

Acknowledgments The CLASH program (GO-12065) is based on observations made with the NASA/ESA *Hubble Space Telescope*. The Space Telescope Science Institute is operated by the Association of Universities for Research in Astronomy, Inc. under NASA contract NAS 5-26555. This work is also based in part on archival data obtained with the *Spitzer Space Telescope*, which is operated by the Jet Propulsion Laboratory, California Institute of Technology under a contract with NASA.

Author Contributions W.Z. made the initial identification and wrote a draft. R.B., D.C., H.F. and L.B. verified the target selection. M.P. and H.F. performed comparisons with intermediate-redshift and nearby objects and edited the final version. W.Z., A.K., L.B., D.C., S.O. and E.M. processed the *HST* data. X.S., W.Z. and L.A.M. performed the IRAC photometry. S.J., A.M., D.C., O.H. and N.B. made the redshift estimates. M.P., T.R.L. and L.B. performed the image deconvolution. J.M. carried out the SED fitting. A.Z., M.C. and T.B. ran the lensing models. The above authors also contributed the text and figures that describes their analyses. P.R., L.I., P.M., M.N., R.B. and L.A.M. contributed to the observing programs. M.B., M.D., C.G., S.J., D.D.K., O.L., D.L., P.M., K.U. and A.W. helped with the manuscript.

Correspondence Correspondence and requests for materials should be addressed to W.Z. (email: zheng@pha.jhu.edu).

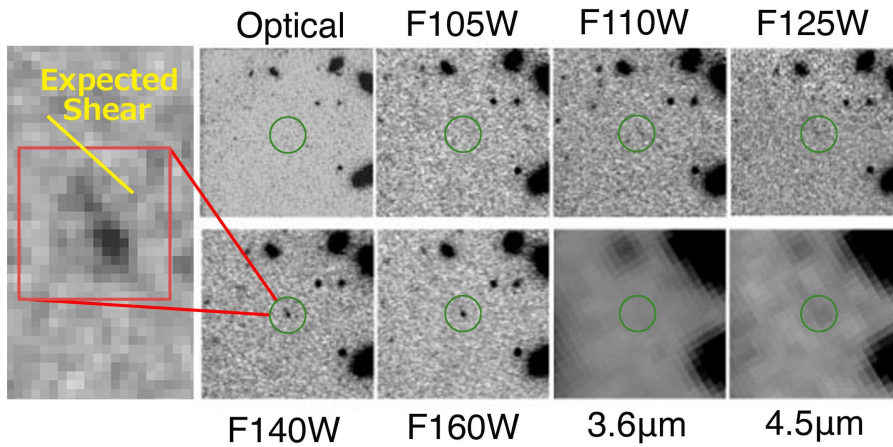


Figure 1 – Cutout images of MACS1149-JD1 in the optical (ACS, summed), near-infrared (WFC3) and infrared (IRAC) bands. Each image is 10'' on one side. North is up and east to the left. The source, located at the center of each image, is firmly detected in the F140W (1400 nm) and F160W bands and weakly detected in the F110W, F125W and 4.5 μ m bands. An enlarged view of the F140W image shows its elongation, which is extended along a position angle of ~ 37 degrees. A yellow line marks the direction of shear predicted by the lensing model.

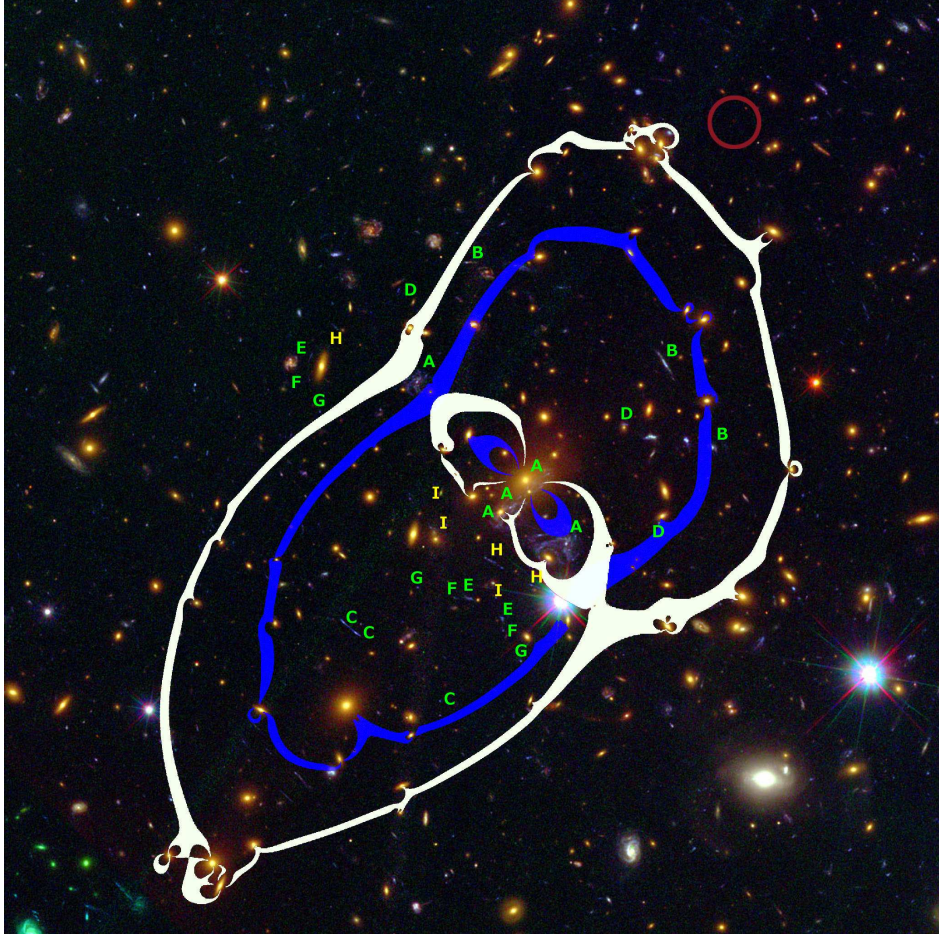


Figure 2 – Composite color image of MACS J1149.6+2223. North is up and east to the left. The field of view is 2.2 arcmin on each side. The $z = 9.6$ critical curve for the best-fit lensing model is overplotted in white, and that for $z = 3$ is shown in blue. Green letters A-G mark the multiple images of seven sources that are used in the strong-lensing model. Yellow letters H and I mark the two systems that are not used in the final fitting. The location of MACS1149-JD1 is marked with a red circle, at RA= $11^h49^m33^s.584$ Dec= $+22^\circ24'45''.78$ (J2000).

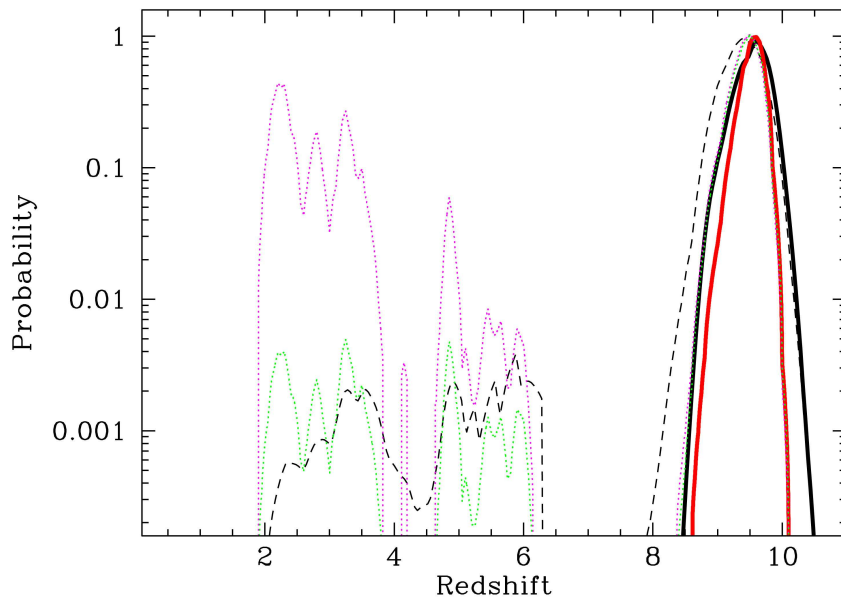


Figure 3 – Probability distribution of photometric redshift estimation. All curves are normalized to their peak probability. Solid black curve: LPZ, using all the *HST* and *Spitzer* data; Solid red curve: BPZ with and without priors, using all data. Only the high-redshift solutions are confirmed with high confidence ($> 4\sigma$). Dashed black curve: LPZ, using the *HST* data only. Dotted green curve: BPZ without priors, using the *HST* data only. In these two cases, intermediate-redshift solutions are present at low probability ($< 1\%$). Dotted magenta curve: BPZ with priors, using the *HST* data only. Only in this case intermediate-redshift solutions become significant.

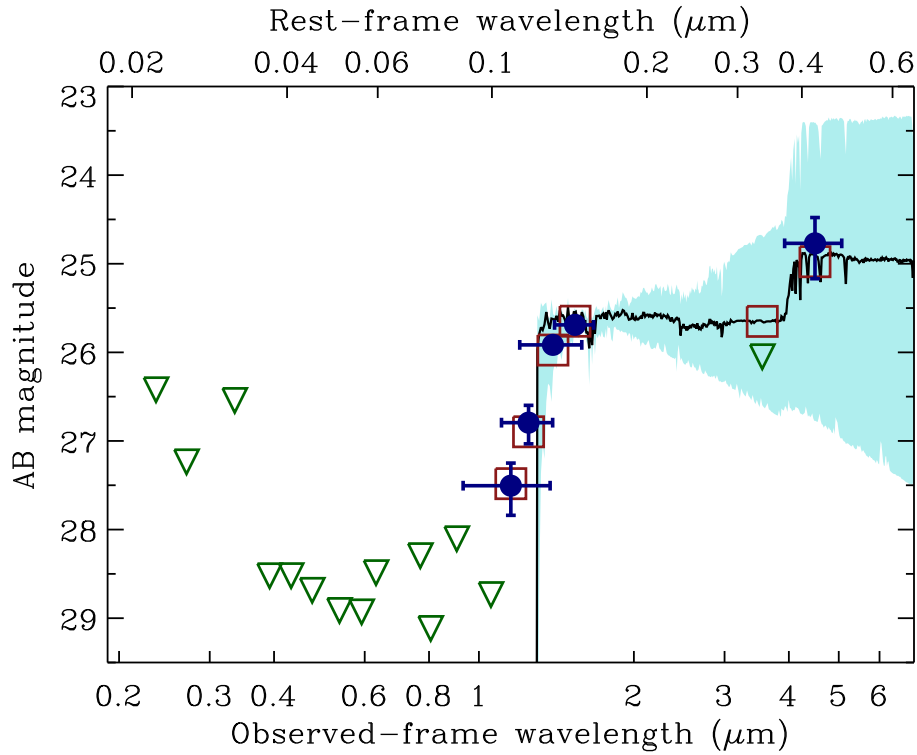


Figure 4 – Stellar population synthesis modeling results for MACS1149-JD1. The filled blue points mark bands in which the object is detected, while the open green triangles indicate 1σ upper limits. The errors in the F140W and F160W bands are small (<0.1 magnitude) and hence not visible. The black spectrum is the best-fit model, and the open red squares show the photometry of this model convolved with the WFC3, ACS, and IRAC filter response functions. The light blue shading shows the range of 100 additional models drawn from the posterior probability distribution that are also statistically acceptable fits to the data.

Supplementary information

1. General Outline

MACS1149-JD1 is found in a search of all the observations of 12 CLASH clusters. Its characteristics are described here in further detail, along with our analysis methods. In §2 we describe the *HST* data processing and aperture photometry; in §3 we describe the IRAC photometry that we perform; in §4 we test the intermediate-redshift probability of the source, using only part of the data; in §5 we discuss our lensing model and compare with another independent model; in §6 we describe the *HST* image deconvolution; in §7 we show our SED fitting method; in §8 we demonstrate why the source is not a solar system or Galactic interloper; in §9 we discuss the effect of photometric scattering of intermediate-redshift objects; and in §10 we summarize our tests.

We adopt the cosmological parameters $h = 0.7$, $\Omega_M = 0.3$, and $\Omega_\Lambda = 0.7$.

2. *HST* photometry

The CLASH observations of MACS J1149.6+2223 were made between December 2010 and March 2011. The *HST* images include archival data in the F555W and F814W bands. The data are processed in two independent pipelines: *APLUS*, an enhanced version of *APSYS*³¹ that is now capable of merging and aligning WFC3 images, and *Multidrizzle*^{32,33}. They are combined, aligned and resampled with a common pixel scale of $0''.065$. A Subaru image, centered on the cluster, but covering a 28×28 arcminute field is used as the astrometric reference. Detection images are produced from the combination of ACS (Advanced Camera for Surveys)/WFC and WFC3/IR images. We use the WFC3/IR detection image and run *SExtractor*³⁴ in dual mode in every filter band.

We carry out photometry with circular apertures whose diameter is between 2 and 20 pixels. At larger

apertures, the source flux in each band increases and gradually approaches an asymptotic value. The spectral break becomes less prominent at larger apertures as more noise is added to each band. At each aperture size we estimate the photometric redshift. The most precise photometric redshift is from the photometry made with an aperture of diameter 10 pixels ($0''.65$). To verify the precision, we compare the source counts derived from our two independent pipelines and find that they agree well within the allowance of propagated errors. In the F140W and F160W bands, the count difference is $< 3\%$. The source magnitudes in these two bands are approximately 0.3 magnitude fainter than the values measured at an aperture of 20 pixels. We correct the source magnitude in each *HST* band by -0.3 magnitude (Table 1). For the upper limits in other optical bands, see Fig. 4.

Table 1: Photometry of $z \sim 9.6$ Candidate in MACS J1149.6+2223

F814W	F850LP	F105W	F110W	F125W	F140W	F160W	3.6 μ m	4.5 μ m
$> 29.4^a$	$> 27.9^a$	$> 28.2^a$	27.5 ± 0.3	26.8 ± 0.2	25.92 ± 0.08	25.70 ± 0.07	$> 26.1^a$	24.8 ± 0.3

^a 1σ detection limit.

3. IRAC photometry

We retrieve archival *Spitzer*/IRAC images of MACS J1149.6+2223 observed in July 2010 and February 2011, under Program ID 60034 (PI: Egami), in the form of BCD (Basic Calibrated Data) and PBCD (Post BCD). The BCD data are processed with tasks *Overlap* and *Mosaic* in the MOPEX package to produce the final mosaic images with a pixel scale of $0''.6$. Individual PBCD images serve as the mosaics for each of the two epochs. The exposure times are 33.6 ksec in total and 16.8 ksec on target for both channels at 3.6 and 4.5 μ m.

As the first step, two mosaic images taken at different epochs are used. In both epochs, the cluster is

centered in the Channel 1 ($3.6\ \mu\text{m}$) and 2 ($4.5\ \mu\text{m}$) mosaics. A visual inspection of the independent mosaics at $4.5\ \mu\text{m}$ shows a clear detection at modest significance in both epochs. As the epochs are separated by six months, we rule out the possibility of a spurious detection or a moving object (additional constraints in §8).

The candidate is not visually detected at $3.6\ \mu\text{m}$ in either epoch, nor in the total stack, with a 1σ upper limit of magnitude 26.1. The sensitivity of the $3.6\ \mu\text{m}$ mosaic images is estimated by measuring the standard deviation of flux values in $2''.4$ -diameter apertures randomly placed on empty background regions. The IRAC photometry at $4.5\ \mu\text{m}$ is carried out in several ways. We run *GALFIT*³⁵ to fit the brightness profile of MACS1149-JD1 and neighboring sources simultaneously. The PSF image is made from the $4.5\ \mu\text{m}$ mosaic image by stacking four bright (magnitude ~ 18.5) and isolated stars. For bright neighboring foreground galaxies which cannot not be satisfactorily fitted with a pure PSF model, we assume a generalized Sérsic profile and use the higher-resolution *HST*/WFC3 *H*-band image as a reference for the initial *GALFIT* input parameters.

Because of the importance of photometry in the $4.5\ \mu\text{m}$ band, we perform extensive tests to calibrate it. We construct simulated point sources convolved with the IRAC PSF profile and normalized to magnitudes of 24.0, 24.5 and 25.0, respectively. We place these simulated sources in the vicinity of MACS1149-JD1, and run *GALFIT* with different fitting windows (Fig. 5) until the expected magnitude of each simulated source is recovered. We proceed to fit the flux of MACS1149-JD1 without simulated sources, using the fitting window and background level on the image that recovered the brightness of the simulated sources most accurately. We repeat these tests at five different positions for the simulated sources of three different magnitudes to verify the measurements of the source magnitude. To account for the uncertainties in estimating the background at different positions around MACS1149-JD1, we choose their mean value of 24.77 ± 0.3 as the source magnitude in the $4.5\ \mu\text{m}$ band.

We then use the above *GALFIT* results to subtract out the neighboring sources (but not MACS1149-JD1 itself), and perform aperture photometry using $2''.4$ diameter apertures. The local background is determined from an annulus of radius between 4 and 10 pixels. We find the source magnitude 26.0 ± 0.3 , subject to a correction of -0.7 magnitude for the missing flux outside the aperture³⁶. This magnitude derived from a small aperture is fainter by approximately 0.5 magnitude than that from *GALFIT* fitting. Note that the median of the pixel values in the sky annulus is used for the background estimation. We verify that the measured source flux could increase by $\sim 0.1 - 0.2$ magnitude if a smaller annulus for the sky is used (*e.g.* an outer radius of 8 pixel) to avoid the possible contamination from a few brighter pixels. While the measurement supported the *GALFIT* results that the source is detected, we do not use this value in Table 1 because of its larger uncertainty.

4. Intermediate-redshift probability

While our most probable and robust photometric redshift estimations yield the high-redshift solution (Fig. 3), we further study alternative solutions when the IRAC data are not used in the fitting. Intermediate-redshift solutions are found at low probability when we run LPZ and BPZ with only the four WFC3/IR bands where the source is detected. However, these intermediate redshift solutions all have considerably higher χ^2 values than the best fit solution at $z = 9.6$. For each model used, we calculate the χ^2 value from the estimations. LPZ yields a best-fit model for a starburst galaxy at $z = 9.63 \pm 0.25$ with a low $\chi^2 = 0.37$. We find a secondary solution for an elliptical galaxy at $z \sim 5.92$ with a $\chi^2 = 1.74$. While this second solution is within 1σ from the best-fit value, it requires a model with an old stellar population – an unlikely scenario at $z \sim 6$. Fig. 6 shows the χ^2 values as a function of redshifts and the types of galaxy templates as the LPZ output. Intermediate-redshift solutions yield considerably higher χ^2 values and are hence unlikely.

5. Lensing model

The basic assumption in our SL modeling approach is that light traces mass, so that the photometry of red sequence cluster members constitutes the starting point of modeling. We use the spectroscopic redshifts¹⁴ and the accurate photometric redshifts derived via the CLASH multiband imaging. The mass model for each red sequence member is based on a surface-density power law, scaled by the galaxy’s luminosity. The superposition of these power laws represents the lumpy, galaxy-scale mass component. This component is then smoothed by fitting a low-order polynomial to it, via 2D spline interpolation, whose result constitutes a smooth DM component. In total there are six fundamental free parameters²²: the galaxy power law and the smoothing (polynomial) degree are the first two free parameters. The two mass components are then added with a relative galaxy-to-DM weight, which is the third free parameter. To the resulting deflection field, we add an external shear describing the overall ellipticity. The direction of the external shear and its magnitude are two additional free parameters. The overall scaling of the mass model is the last free fundamental parameter.

We generate preliminary mass models expanding the six parameter space, which, along with the CLASH imaging and photometric redshifts, help examine the multiple images and candidates presented in previous work^{13, 14} and identify two new candidate systems (although these are not used for the minimization). The minimization for the final best-fit models is then implemented via a Monte Carlo Markov Chain (MC) with the Metropolis-Hastings algorithm³⁹ whose final results we use here. The chain includes six free parameters: the relative weight of the bright central galaxy and five other bright galaxies in the field, which allows for a more accurate determination of the very inner mass profile. In addition, we allow the redshift of the four systems with photometric redshifts to vary and be optimized by the model, introducing four additional free parameters.

The MC chain then minimizes 16 free parameters, and includes (after burn-in) a total of 20,000 steps with a typical $\sim 20\%$ acceptance rate. Estimating the goodness-of-fit of the best-fit model from

this chain (where throughout we adopt a $\sigma = 1''.4$ as the positional error in the χ^2 term), the χ^2 and root-mean-square (rms) are 61.77 and $1''.92$, respectively. As constraints for the minimization, we use 23 secure multiple images of seven sources, whereas for system 1 as defined by Zitrin & Broadhurst¹³, we use several distinctive knots across these large images as additional constraints. In total, we use 37 image+knots positions as constraints. The best-fit model yields a $\chi_{red}^2 = 2.06$ and a magnification of $14.5^{+4.2}_{-1.0}$, while the median magnification from the MC chain is slightly higher: $15.5^{+3.3}_{-1.9}$.

In addition, we also generate a `Lenstool` mass model^{23,40} to compare with our findings. The mass distribution and profile of the main halo are obtained by fitting the multiple-image information to a Navarro-Frenk-White profile⁴¹. We include the contribution of the brightest cluster galaxy (BCG) and the 187 brightest member galaxies modeled by a truncated pseudo-isothermal elliptic mass distribution⁴². As constraints for the minimization, we use 21 secure multiple images of seven sources, adopting a $\sigma = 1''$ as the positional error. The goodness-of-fit for this model of the 10,000 accepted samples is $\chi_{red}^2 = 2.19$, with an rms error of image positions of $1''.71$ in the image plane. It therefore constitutes another independent measure, based on the adopted profile model that is different than our light-traces-mass assumption. With this best-fit model we find a magnification of $26.6^{+20.8}_{-7.7}$ for MACS1149-JD1.

The magnification and shear of the two models agree within the statistical errors. However, the value of the magnification factor close to the critical curves is a quantity sensitive the model details, and one has to also examine possible systematics. The comparison of the two modeling methods allows us to estimate a systematic uncertainty of order of $\Delta\mu \sim 5$. Secondly, we check the effect of the weight (or, the mass-to-light ratio) of the bright group of galaxies a few arcseconds south-east of the $z \simeq 9.6$ candidate image, since this could have a strong effect on the resulting magnification, and these are fixed in both models. Correspondingly, we find that a reasonable 20% variation in the weights of these galaxies entail a magnification change of $\Delta\mu \sim 5$. To further examine possible systematics in the two methods, we generate

two independent models using `Lenstool` (the first includes one central DM component, while the other which we incorporate here, models the cluster as two DM clumps), and several independent models using the method of Zitrin et al. (2011)²², each with a different combination of free parameters (*i.e.*, different galaxies freely weighted, or photometric redshift optimizations). By doing so, we have a set of models to compare to the best fitting model used above, and assess the systematics these changes entail. We note that some of these resulting models have critical curves (where the magnification diverges) that pass through the image or further outwards of its location, so that in principle, the upper systematic limit on the best-fit model magnification, is poorly constrained. Both of these models have in general a lower reduced χ^2 than the complementary chain models, and in particular, yield better reproduction of images, as gauged by visual inspection. These are therefore chosen as the best-fit models used above whose values we adopt throughout. We conclude that systematic uncertainties are of the same order as the statistical uncertainties, albeit with poorly constrained upper limits.

Our best fit lens model predicts that MACS1149-JD1 lies outside the caustics for $z \sim 10$ in the source plane, so that it is likely not to be multiply-lensed, but it is still predicted to be significantly magnified by gravitational lensing from the cluster. To examine the possibility of multiple images, we choose a complementary MC chain model with somewhat a different combination of free parameters that does predict multiple images. No counter images brighter than magnitude 27 are found in the area where counterpart images are predicted.

Both lensing models predict a highly elongated image. Although the observed source is elongated along in the direction predicted by the lensing model, the level of elongated is lower than the model predictions. As a result, the intrinsic image in the source plane is not circular. However, as the magnification especially close to the critical curves is one of the more sensitive quantities to measure, this probably results from statistical and potential systematic uncertainties in lens modeling. We anticipate future improvements

in modeling to reduce such potential systematic errors.

6. Image Deconvolution

The drizzled F160W-band image is deconvolved using 20 iterations of Lucy-Richardson deconvolution^{37,38}. The PSF is provided by a bright field star within the stacked image displaced $39''$ from the object. This is a modest amount of deconvolution, but is sufficient to remove the blurring due to the PSF wings, and to provide a model-independent representation of the object.

After deconvolution, the extent of the source is significant out to $\approx 0''.3$ from its center. The distribution of light for $0''.13 \leq r \leq 0''.33$ is roughly exponential with a scale length of $0''.067 \pm 0''.005$. The isophote ellipticity over the region fitted increases with radius to ~ 0.5 . at $r = 0''.33$. The half-light radius of the source is $r < 0''.13$.

Using the detailed lens model for MACS J1149.6+2223 and the PSF-deconvolved F160W image, we reconstruct the MACS1149-JD1 image in the source plane at $z = 9.6$. The source-plane reconstruction is shown in Fig. 7. The candidate is significantly elongated in the source plane along a position angle of 139 degrees and is well-fit by a 2D Gaussian. The Gaussian fit shows that the candidate has an axis ratio of 7.55. Assuming $4.28 \text{ kpc arcsec}^{-1}$ at $z = 9.6$, the source spans 1.28 kpc and 0.17 kpc along its major and minor axis, respectively. Note that the most significant elongation is in the F140W band.

7. Spectral Energy Distribution Modeling

Our SED modeling constructs a large suite of models using Monte Carlo draws of the free parameters, and then evaluates the posterior probability distribution of each parameter by calculating the statistical likelihood of each model. To fit MACS1149-JD1 we synthesize photometry in the 19 observed bands for 50,000 models assuming a fixed redshift of $z = 9.6$. We parameterize the star formation history $\psi(t)$ as

a delayed τ model, $\psi(t) \propto t \exp(-t/\tau)$, where t is the time since the onset of star formation and τ is a characteristic time scale. The advantage of this parameterization is that it allows for both linearly rising ($t/\tau \ll 1$) and exponentially declining ($t/\tau \gg 1$) star formation histories. We draw τ from a uniform distribution of between 10 Myr and 1 Gyr, t uniformly from 5 – 500 Myr, and the stellar metallicity in the range $Z = 0.002 - 0.02$ (10% – 100% solar). For our fiducial modeling we assume no dust obscuration, although we test the effect of relaxing this assumption below.

Fig. 8 shows the posterior probability distributions on the stellar mass, star-formation rate (SFR), and SFR-weighted age, $\langle t \rangle_{\text{SFR}} \equiv \int_0^t \psi(t')(t - t') dt' / \int_0^t \psi(t') dt'$. Since we are unable to place any significant constraints on either τ or the metallicity Z , we do not show these probability distributions here. Based on the median of the posterior probability distributions, our Bayesian analysis suggests a stellar mass of $\sim 1.5 \times 10^8 (\mu/15)^{-1} M_\odot$ for MACS1149-JD1, and a SFR of $\sim 1.2 (\mu/15)^{-1} M_\odot \text{ yr}^{-1}$. Although the probability distribution on $\langle t \rangle_{\text{SFR}}$ is not peaked, we find that 95% of the models have $\langle t \rangle_{\text{SFR}} < 200$ Myr, suggesting a likely formation redshift $z_f < 14.2$. This analysis clearly demonstrates the need for precise IRAC photometry of high-redshift galaxies, in order to place their physical properties on firmer quantitative footing.

We investigate the effect of changing our prior assumptions on these results. First, we consider an ensemble of models that includes dust, allowing the rest-frame V -band attenuation⁴³ to range from 0 – 2 magnitude. This analysis yield median stellar mass and SFR estimates that are a factor of ~ 6 higher, but with no improvement in the likelihood, and no constraint on the V -band attenuation. However, our constraints on z_f change by $< 5\%$. We also consider simple exponentially declining star formation histories; those yielded similar estimates for the stellar mass and SFR (within a factor of ~ 2) with respect to our fiducial model parameters, and constrain the formation redshift to $z_f < 17.5$.

We also test the possibility that MACS1149-JD1 is an intermediate-redshift interloper (see Fig. 9). Assuming a representative value of $z = 3.2$ (Fig. 3 and 6), we construct a suite of 50,000 models with exponentially declining star formation histories spanning a wide range of stellar metallicity ($0.0002 - 0.03$), dust attenuation ($A_V = 0 - 3$ magnitude), age (5 Myr to 2 Gyr, where 2 Gyr is the age of the Universe at this redshift), and τ ($0.01 - 10$ Gyr). Assuming an intermediate-redshift solution, the best-fit model has a reduced $\chi^2 = 4.1$, compared to $\chi^2 = 1.4$ when assuming a redshift $z = 9.6$. In addition, as shown in the inset to Fig. 9, the χ^2 distribution of the full suite of models assuming $z = 9.6$ all peak around $\chi^2 \approx 1.5$ (light blue histogram), whereas the χ^2 distribution of the bulk of the models assuming $z = 3.2$ are centered around $\chi^2 \approx 9$ (gray histogram). This analysis demonstrates that the high-redshift solution is clearly preferred from the point-of-view of the SED modeling.

The age estimate of high-redshift galaxies is useful, as magnified sources make it significantly easier to carry out *Spitzer*/IRAC photometry. Without the lensing effect, the rest-frame optical flux would be virtually impossible to measure for galaxies at $z > 8$, as the anticipated fluxes in the IRAC bands are below the IRAC confusion limits. Fig. 10 plots the *HST* and IRAC magnitudes for a number of objects²⁹ at $z \sim 7 - 8$. Our measurements are consistent with the result, but with considerably higher accuracy at the source's intrinsic magnitude, thanks to the gravitational magnification.

8. Solar System and Galactic Interlopers

We demonstrate here that the likelihood that MACS1149-JD1 is either a faint solar system or Galactic object is extremely low. CLASH observations of MACS J1149.6+2223 were obtained at eight different epochs and our F140W and F160W images, in particular, cover five of those epochs spanning 80 days between December 20, 2010 and March 10, 2011. At each epoch, we measure the relative separation between MACS1149-JD1 and a bright early type galaxy with a compact core that is $\sim 10''$ away. This

galaxy provides our common stationary astrometric reference point. The relative offsets, as a function of time, with respect to the mean separation between MACS1149-JD1 and the reference galaxy are shown in Fig. 11. Based on these measurements, the proper motion of the source is $< 0''.13$ per year. If MACS1149-JD1 were an object on a low-eccentricity orbit within the solar system, its orbital period would have to be in excess of 10 million years - implying an orbital semi-major axis that is at least two orders of magnitude beyond the distance of Kuiper belt and Trans-Neptunian objects (40 – 100 AU). Only objects in the Oort cloud ($\sim 50,000$ AU) would be expected to have such small proper motions but both the predicted absolute magnitudes and colors of typical Oort cloud objects⁴⁴ would be inconsistent with those of MACS1149-JD1 (MACS1149-JD1 is about 9 magnitudes brighter than what is expected for a 20 km wide Oort cloud object).

To assess whether MACS1149-JD1 could be a cool Galactic star, we compare its colors to a sample of 75 stellar templates of L,M,T dwarfs compiled from a spectral atlas^{45,46} and Y dwarfs from stellar model atmospheres⁴⁷. For each star we compute its predicted flux in F814W, F105W, F110W, F125W, F140W, F160W, IRAC 3.6 μm and 4.5 μm bands and normalize the fluxes so they match the F160W measurement for MACS1149-JD1. We then compute, for each star, the corresponding total flux deviation from the MACS1149-JD1 flux values using the expression:

$$\langle \Delta f \rangle = \sqrt{\sum_{i=1}^N [(f_{i,MACS1149-JD1} - f_{i,STAR})/\sigma_{i,obj}]^2} \quad (1)$$

where the sum is over the eight bands. There are no L,M,T, or Y dwarfs whose total flux difference is within 6σ of the observed colors of MACS1149-JD1 (see also Fig. 12). Indeed, the minimum difference in flux space between the source and the closest stellar match is 6.8σ and the median difference is 16.8σ . The combination of NIR detections and upper limits measured for MACS1149-JD1 thus argues strongly against a cool, faint Galactic star as the likely explanation for the source.

9. Photometric Scatter Test

We demonstrate that the photometry of MACS1149-JD1 is not likely to be due to drawing randomly from the main faint galaxy population. We extract from all 12 CLASH cluster object catalogs derived from IR-based detection images those sources that have approximately similar WFC3 F160W fluxes as MACS1149-JD1. The selection criterion is $25.45 < F160W \leq 26.95$. There are a total of 5614 objects that satisfy this criterion. We then generate new magnitudes for each object by randomly drawing, from a Gaussian distribution, with a mean equal to the object’s measured flux and with a standard deviation equal to the object’s flux uncertainty. We then count how many such objects would have measured flux ratios that lie within the 1σ uncertainty of the F110W/F125W and F125W/F160W flux ratios of MACS1149-JD1 and that also show no flux (at the 2σ level) in the F814W and F105W bands. We run 1000 such realizations of the sample and find that only 0.015% of the objects (averaged over 1000 realizations) would satisfy these criteria. Thus, MACS1149-JD1 is unique amongst the population of faint sources at the 99.985% level (Fig. 13).

10. Summary

We carry out extensive analyses to study the nature of such an object with unique properties and found the following evidence:

- Detection of the source at multiple epochs in both *HST* and *Spitzer* imaging rules out the source being a spurious detection or a transient object.
- The combination of color decrements at $\sim 1.3 \mu\text{m}$ and $\sim 4 \mu\text{m}$ favor a high-redshift solution
- Intermediate-redshift fits yield significantly higher values of χ^2 using just *HST* photometry alone.
- Intermediate-redshift solutions are ruled out at 4σ when *HST* and *Spitzer* photometry are used in photometric redshift estimation.

- The de-lensed magnitude is consistent with expectations for sources at $z > 8$.
- The de-lensed half-light radius is more consistent with expectations for sources at $z > 8$.
- The source plane morphology is significantly more elongated than the image plane morphology.
- The proper motion upper limit and the source's apparent magnitude make it very unlikely that the source is a Kuiper Belt, Trans Neptunian or Oort cloud object.
- Location of the source in multi-color space is inconsistent (at 4σ) with the source being a cool Galactic dwarf star (spectral type L,M,T,Y).
- Photometric scatter is not sufficient to explain colors, and this explanation is rejected at the 99.985% confidence level.

We therefore conclude that the MACS1149-JD1 is very highly unlikely to be an intermediate-redshift interloper, a cool, late-type star, or solar system object. The most probable explanation would seem to be a $z = 9.6$ galaxy.

31. Blakeslee, J. P., Anderson, K. R., Meurer, G. R., Benítez, N., & Magee, D. An automatic image reduction pipeline for the advanced camera for surveys, in *Astronomical Data Analysis Software and Systems XII* (San Francisco: ASP), eds. H. E. Payne, R. I. Jedrzejewski, & R. N. Hook, **295**, 257-260 (2003)
32. Koekemoer, A. M., Frutcher, A. S., Hook, R. N., & Hack, W. MultiDrizzle: an integrated pyraf script for registering, cleaning and combining images, in *The 2002 HST Calibration Workshop: Hubble after*

- the Installation of the ACS and the NICMOS Cooling System*, ed. S. Arribas, A. Koekemoer, & B. Whitmore, 337-340 (2002)
33. Koekemoer, A. M., et al. CANDELS: the cosmic assembly near-infrared deep extragalactic legacy survey - the Hubble space telescope observations, imaging data products, and mosaics, *Astrophys. J. Suppl.*, **197**, 36 (2011)
 34. Bertin E., & Arnouts S. SExtractor: software for source extraction, *A&Ap*, **117**, 393-404 (1996)
 35. Peng, C. Y., Ho, L. C., Impey, C. D., & Rix, H.-W. Detailed structural decomposition of galaxy images, *Astron. J.*, **124**, 266-293 (2002)
 36. Eyles, L. P., et al. Spitzer imaging of i'-drop galaxies: old stars at $z \sim 6$, *Mon. Not. R. Astron. Soc.*, **364**, 443-454 (2005)
 37. Lucy, L. B. An interactive technique for the rectification of observed distributions, *Astron. J.*, **79**, 745-753 (1974)
 38. Richardson, W. H. Bayesian-based iterative method of image restoration, *J. Opt. Soc. A.*, **62**, 55-59 (1972)
 39. Dunkley, J., Bucher, M., Pedro G., Ferreira, P. G., Moodley, K., & Skordis, C. Fast and reliable Markov chain Monte Carlo technique for cosmological parameter estimation *Mon. Not. R. Astron. Soc.*, 356, 925-936 (2005)
 40. Kneib, J.-P., Mellier, Y., Fort, B., & Mathez, G. The Distribution of dark matter in distant cluster lenses - modelling A370, *A&Ap*, **273**, 367-376 (1993)
 41. Navarro, J. F., Frenk, C. S., & White, S. D. M. The Structure of cold dark matter halos, *Astrophys. J.*, **463**, 563-575 (1996)

- 42. Limousin, M., Kneib, J.-P., & Natarajan, P. Constraining the mass distribution of galaxies using galaxy-galaxy lensing in clusters and in the field, *Mon. Not. R. Astron. Soc.*, **356**, 309-322 (2005)
- 43. Calzetti, D., et al. The dust content and opacity of actively star-forming galaxies, *Astrophys. J.*, 533, 682-695 (2000)
- 44. Sheppard, S. S. The colors of extreme outer solar system objects, *Astron. J.*, **139**, 1394-1405 (2010)
- 45. Rayner, J. T., Cushing, M. C. & Vacca, W. D. The infrared telescope facility (IRTF) spectral library: cool stars, *Astrophys. J. Suppl.*, **185**, 289-432 (2009)
- 46. Cushing, M. C., Rayner, J. T. & Vacca, W. D. An infrared spectroscopic sequence of M, L, and T dwarfs, *Astrophys. J.*, **623**, 1115-1140 (2005)
- 47. Huber, I. & Burrows, A. A systematic study of departures from chemical equilibrium in the atmospheres of substellar mass objects, *Astrophys. J.*, **669**, 1248-1261 (2007)

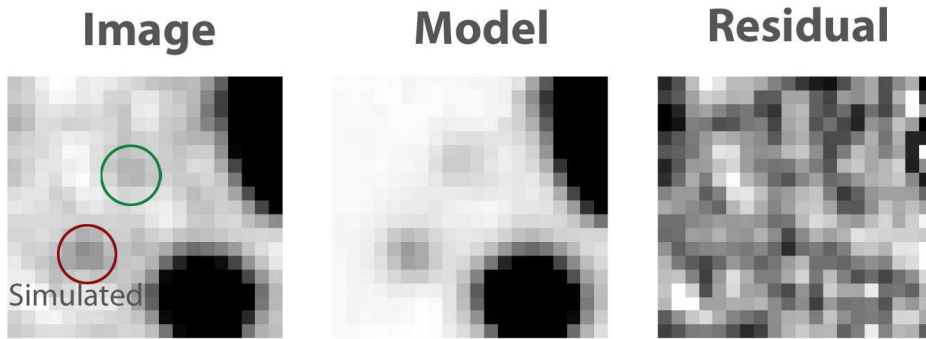


Figure 5 – Illustration of IRAC fitting at $4.5\mu\text{m}$. In the left panel, MACS1149-JD1 is marked with a green circle, and a simulated point source of $AB=24.0$ is marked with a red circle. In the middle panel, the best-fit *GALFIT* model is displayed, and in the right panel, the residual image with all model components subtracted. Note that the actual fitting is made without simulated sources and yields a mean magnitude of 24.8 ± 0.3 .

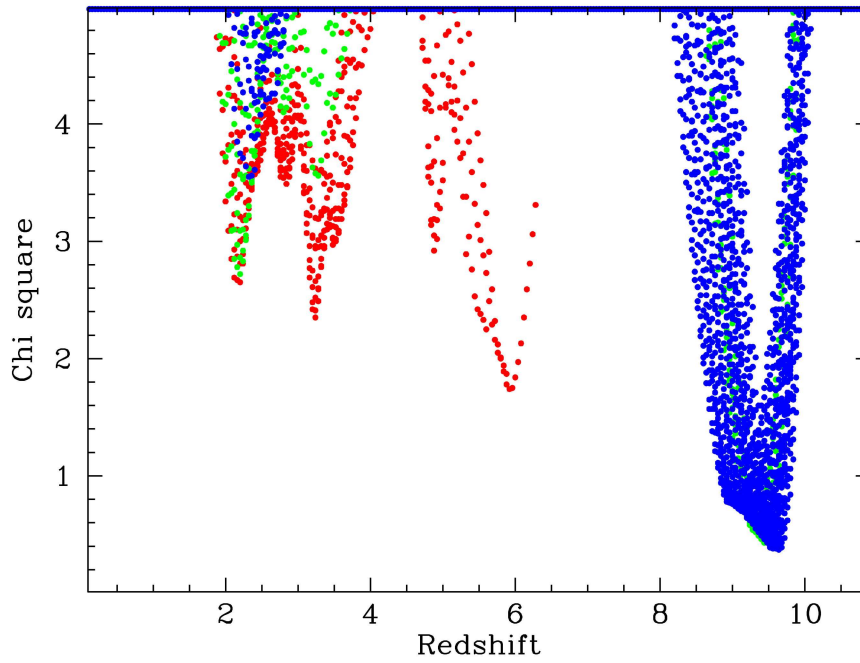


Figure 6 – Likelihood distribution of photometric redshift. We fit only the four *HST* bands where the source is detected, and then plot the χ^2 values at different fitted redshifts for each template in the LPZ template library, plus the effect of dust attenuation. χ^2 values higher than 5 are truncated. Green points: elliptical galaxies; red points: spiral galaxies; and blue points: starburst galaxies, some of which yield the lowest χ^2 values. Intermediate-redshift solutions yield considerably higher χ^2 values than the high-redshift solutions.

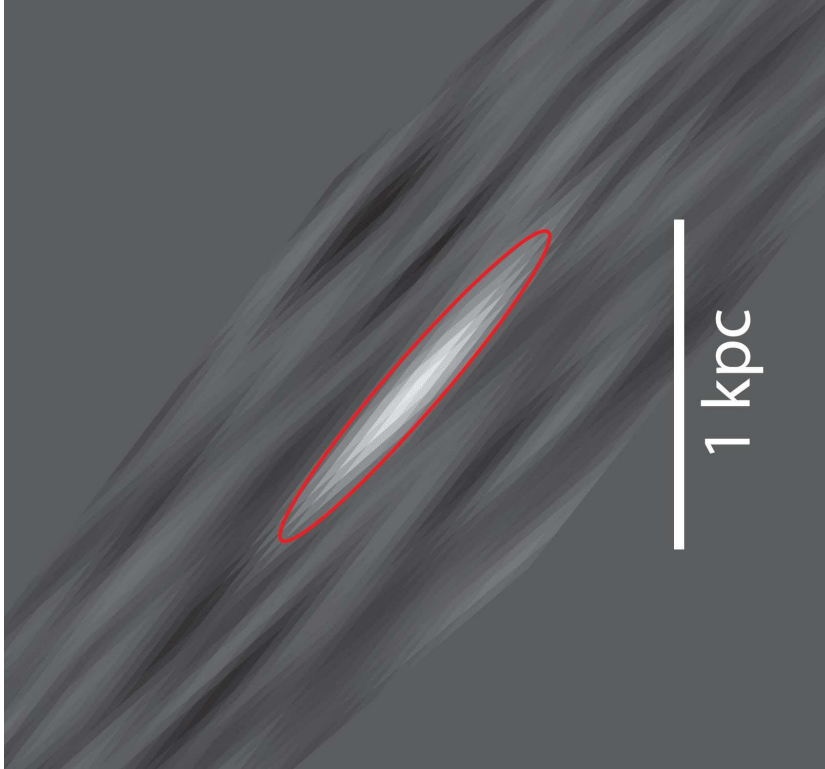


Figure 7 – Source-plane reconstruction of MACS1149-JD1 in the WFC3/IR F160W band. The source is significantly elongated with an axis ratio of 7.55. The candidate spans 1.28 kpc and 0.17 kpc along its major and minor axis, respectively, as denoted by the red ellipse. The results are sensitive to the model details and systematic errors.

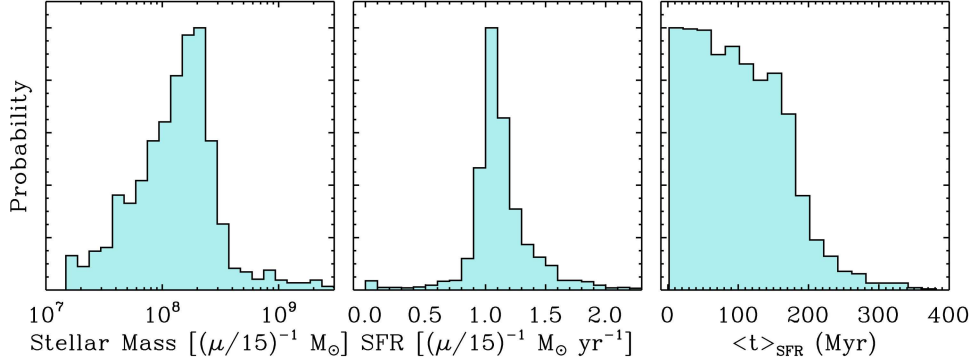


Figure 8 – Posterior probability distributions on the stellar mass, SFR, and SFR-weighted age, $\langle t \rangle_{\text{SFR}}$ based on our Bayesian SED modeling. Note that our stellar mass and SFR estimates have been de-magnified assuming a fiducial magnification factor $\mu=15$, while $\langle t \rangle_{\text{SFR}}$ is independent of μ . Based on this analysis we infer a stellar mass of $\sim 1.5 \times 10^8 (\mu/15)^{-1} M_{\odot}$ a star-formation rate (SFR) of $\sim 1.2 (\mu/15)^{-1} M_{\odot} \text{ yr}^{-1}$, and a constrain on the SFR-weighted age of $< 200 \text{ Myr}$ (95% confidence level), implying a formation redshift $z_f < 14.2$.

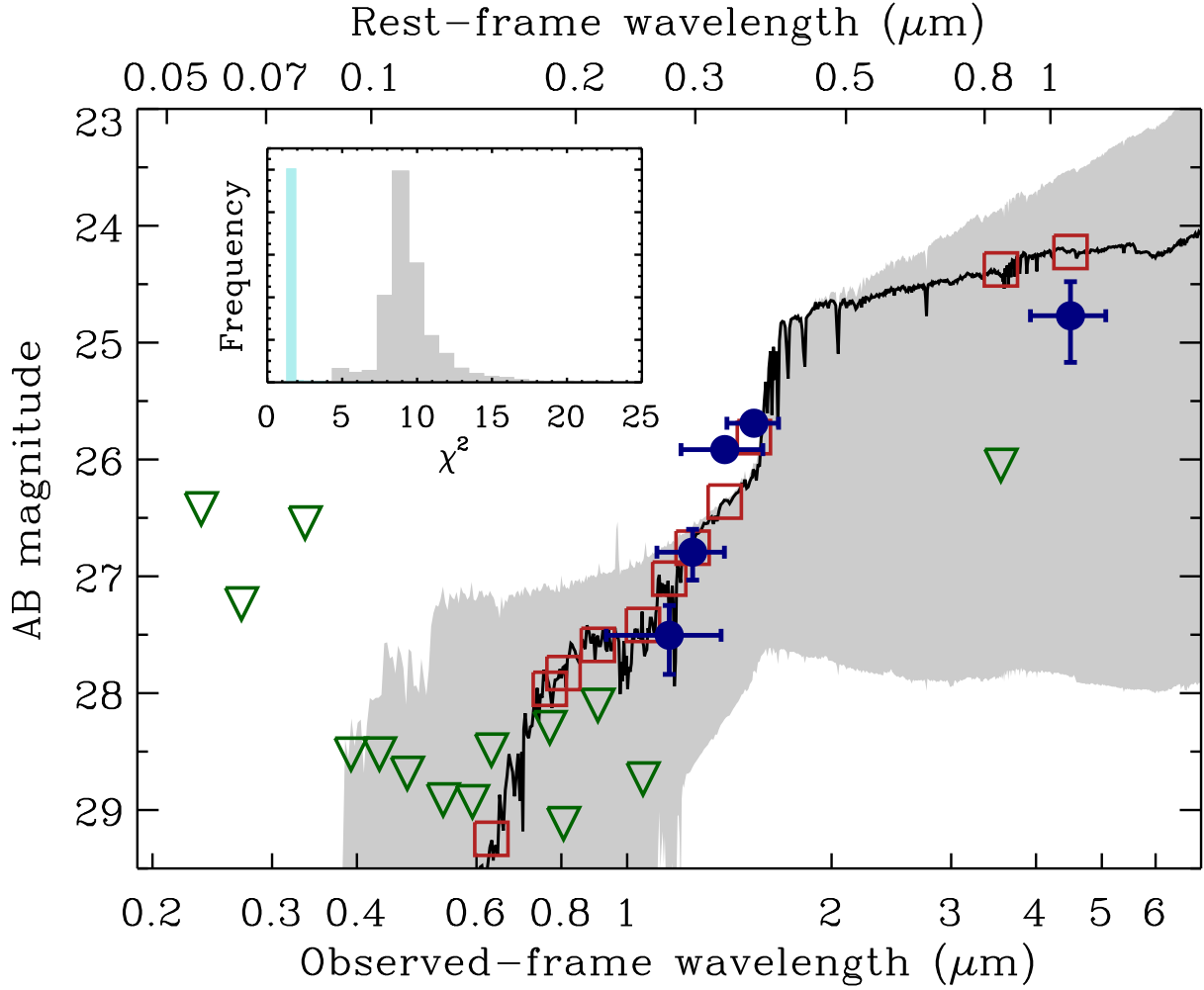


Figure 9 – Results of modeling the SED of MACS1149-JD1 assuming an intermediate-redshift solution, $z=3.2$. This figure is analogous to Fig. 4 but here the gray shading shows the range models drawn from the posterior probability distribution that fit the data assuming $z=3.2$. As shown in the inset, the χ^2 distribution of these intermediate-redshift models peaks around $\chi^2 \approx 9$ (gray histogram), whereas the χ^2 distribution of the models fitted to the data assuming $z=9.6$ peaks around $\chi^2 \approx 1.5$ (light blue histogram; see also Fig. 4). We conclude, therefore, that the high-redshift solution is clearly preferred from the point-of-view of our SED modeling.

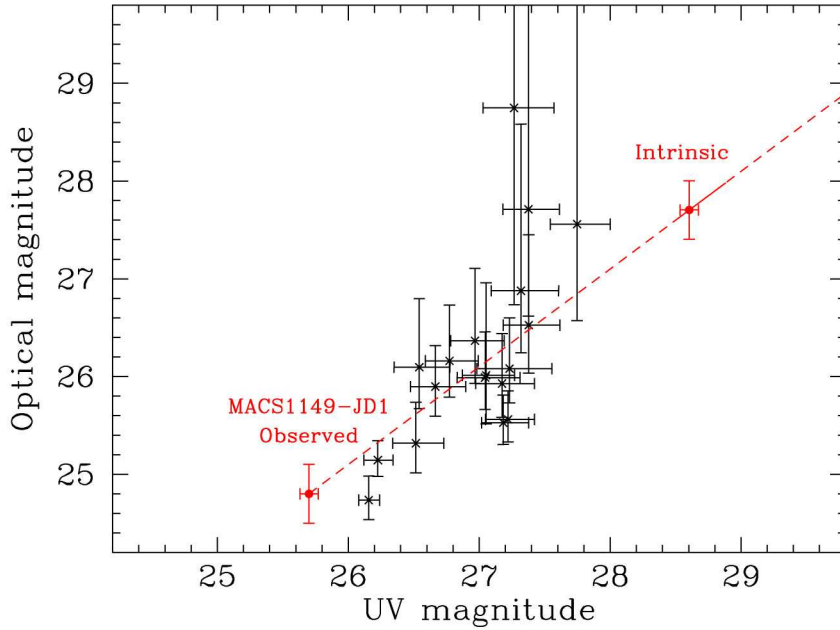


Figure 10 – Rest-frame UV and optical magnitudes of high-redshift objects. The data²⁹ are from objects at $z \sim 7-8$. The rest-frame UV band is F125W, and the rest-frame optical band is the IRAC $3.6\mu\text{m}$. The magnitudes of MACS1149-JD1, in F160W and $4.5\mu\text{m}$ bands, are plotted in red, in their observed values (the lower point) and de-magnified values (scaled down by a flux factor of 15, at the upper-right). The dashed red line is the track of the source’s intrinsic magnitudes under different magnification factors, and the solid red line marks the range for MACS1149-JD1. Cluster lensing makes it possible to improve the accuracy of photometry at the faint end.

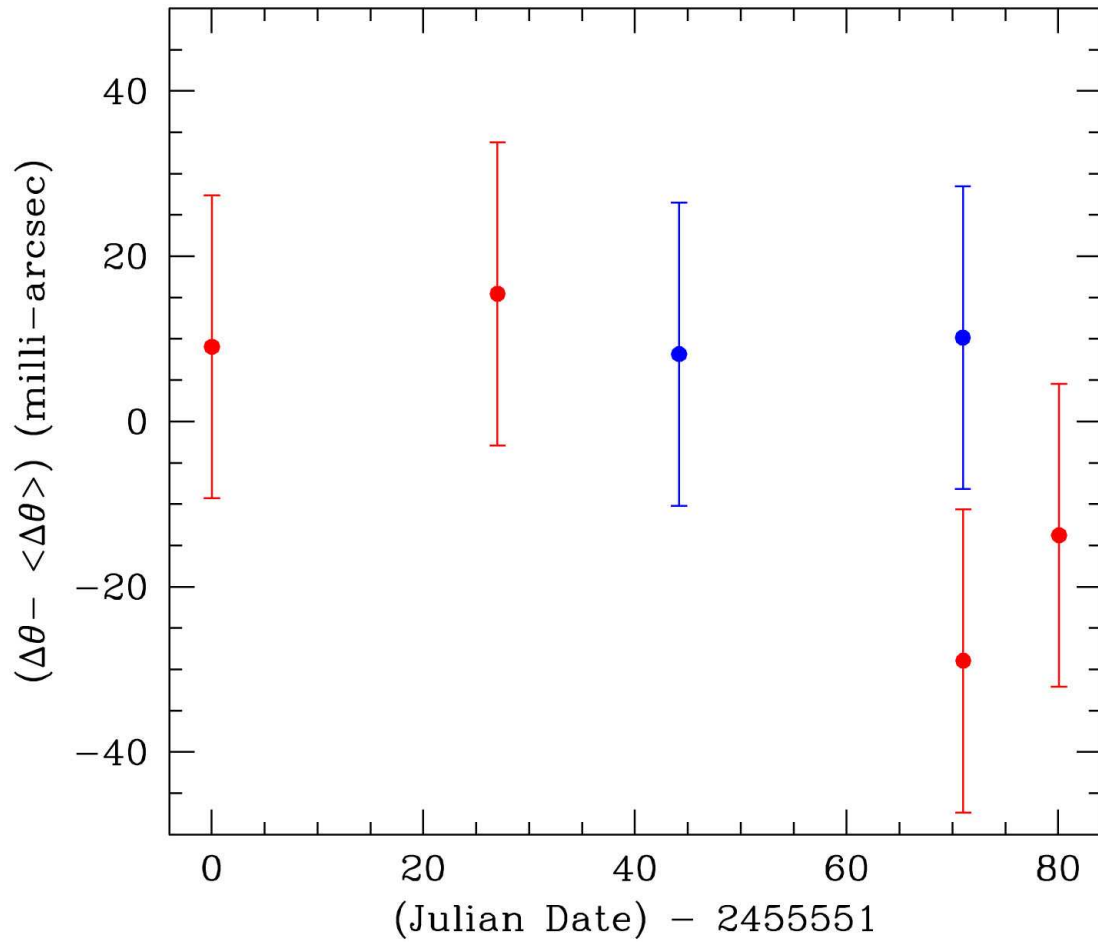


Figure 11 – Relative difference, in milli-arcseconds, between the separation of MACS1149-JD1 from a nearby reference galaxy at each of five separate epochs and the mean separation value. The upper limit on its proper motion is $< 0''.13 \text{ yr}^{-1}$.

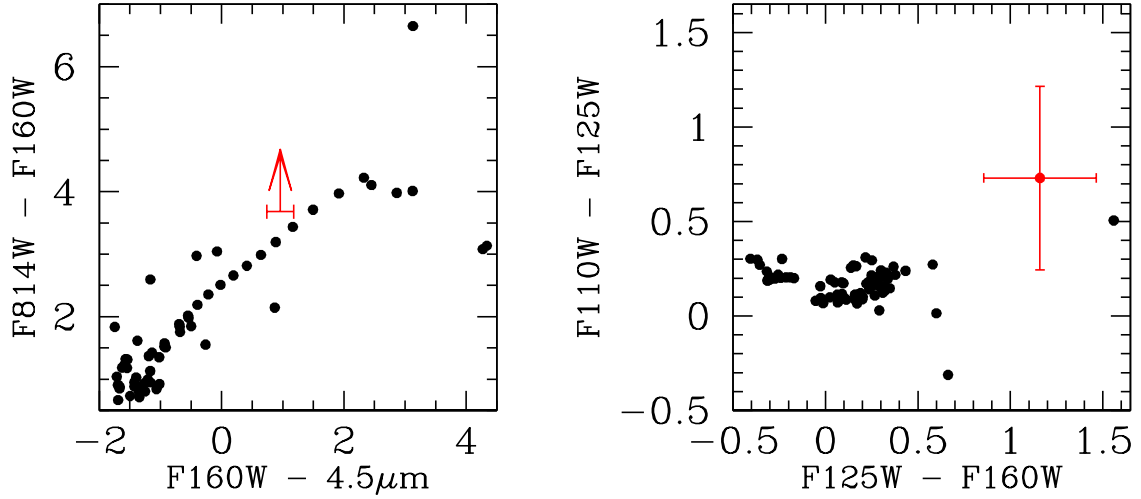


Figure 12 – Comparison of colors of 75 late-type stars^{45–47} (black circles) and those of the high-redshift candidate MACS1149-JD1 (red circle). The $F814W$ magnitude for MACS1149-JD1 is based on its 1σ upper limit. In the right panel, the color of a rare M-8III star is close to the error box, but it is well separated in color in the left panel.

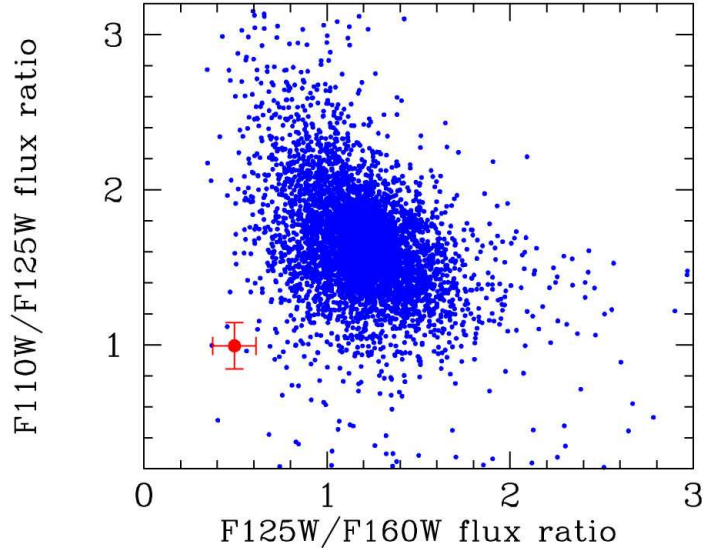


Figure 13 – Flux ratios of faint galaxy population in the CLASH database with F160W magnitude 25.45–26.85. MACS1149-JD1, a resolved source is marked by a red circle. The plotted fluxes are isophotal values and hence are slightly different from Table 1. The five sources next to or within the error box are further examined, and they are rejected because of a detection in optical bands.